

# Evaluation of UAV System Accuracy for Automated Fragmentation Measurement

Thomas Bamford

*Mine Modeling and Analytics Lab, Lassonde Institute of Mining, University of Toronto, Canada*

Kamran Esmaili

*Mine Modeling and Analytics Lab, Lassonde Institute of Mining, University of Toronto, Canada*

Angela P. Schoellig

*Dynamic Systems Lab, Institute for Aerospace Studies, University of Toronto, Canada*

**ABSTRACT:** The current practice of collecting rock fragmentation data is highly manual and provides data with low temporal and spatial resolution. Unmanned Aerial Vehicle (UAV) technology can increase both temporal and spatial data resolution without exposing technicians to hazardous conditions. Our previous works using UAV technology to acquire real-time rock fragmentation data has shown comparable quality results to sieving in a lab environment. However, when applied to a mining environment, it is essential to quantify the accuracy of scale estimation and rock size distribution by considering various sources of uncertainties such as the UAV GPS, which provides noisy measurements. In the current paper, we investigate the accuracy of application of UAVs to collect photographic data for fragmentation analysis. This is done by evaluating the accuracy of the 3D model generated using the UAV system, estimated image scale, and the measured rock size distribution. This paper also investigates the impact of flight altitude on the measured rock size distribution.

## 1 INTRODUCTION

Measurement of muckpile rock fragmentation is important because all downstream mining and comminution process efficiencies are greatly influenced by fragmentation. Mosher (2011) describes that rock fragmentation can influence the volumetric and packing properties of rock and, consequently, the efficiency of digging and hauling equipment. Similarly, other studies have demonstrated the direct influence of the rock size distribution on comminution energy consumption, mill throughput rates and the productivity of these processes (Kanchibotla et al. 1999, McKee 2013). Blasting engineers also use the rock size distribution as a means of quality control of blast design and operation. Thus, the continuous measurement of muckpile rock fragmentation is crucial for the optimization of a mining operation. Despite this importance, the current practice of collecting rock fragmentation data for muckpiles can be logistically complex, laborious, and produces data that has low temporal and spatial resolution (Bamford et al. 2017b).

Unmanned Aerial Vehicle (UAV) technology can increase both temporal and spatial resolution of rock fragmentation data without exposing technicians to hazardous conditions. The added benefit of implementing UAV systems is their capacity to automate

the entire measurement process. Bamford, et al. (2017b) demonstrated that using UAV technology in a laboratory environment to acquire real-time rock fragmentation data has produced comparable quality results to sieving and manual image analysis with significant time savings. This included measuring fragmentation in 20% of the time taken to carry out conventional image analysis. However, in mining environments, there are more measurement uncertainties due to the sensors used and the heterogeneous nature of the muckpiles that are measured. For example, GPS sensors are less accurate than the motion capture system used in the lab. If UAV systems are to be implemented to automate the measurement of muckpile fragmentation in the field, then the quality of results they produce, and their limits should be well understood. The goal of this work is to provide an evaluation of the accuracy of UAV systems for fragmentation data acquisition using photographic methods. Moreover, this work aims to illustrate the impact of UAV flight mission altitude and ground sampling resolution on the minimum detectable particle size using photographic methods.

During a test campaign, rock piles were constructed with sieved rock fragments of different sizes and material types at an active mine site. The rock piles were then measured by a UAV to conduct fragmentation analysis using photographic techniques. Through processing of the collected data, the accuracy of each calculation step to measure frag-

mentation size distribution was computed. This includes calculating the accuracy of the:

- 3D model generated by the UAV system;
- Estimated image scale; and
- Measured rock size distribution.

To illustrate the impact of Ground Sampling Resolution (GSR), the measured rock size distributions for sieved rock piles at two different flight mission altitudes are presented and compared with the screen sizes used to create them.

## 2 FRAGMENTATION MEASUREMENT OF MUCKPILES

Several methods have been developed to estimate rock size distribution for muckpiles. These methods include visual observation by an expert, sieve analysis, and photo (2D) and 3D image analysis. Visual observation involves inspecting the rock pile and subjectively judging the quality of the blasted material. This subjective method often produces inaccurate and imprecise results. Sieve analysis involves

passing a sample of the rock pile through a series of different sieve size trays. This method generates more consistent and accurate results; however, it is more expensive, time consuming, and in certain cases, impractical to perform for muckpiles. Using this method may also result in bias measurement because only a sample of a muckpile can be sieved.

Image analysis techniques for measuring rock fragmentation are commonly used in modern mining operations because they enable practical, fast, and relatively accurate measurements (Sanchidrián et al. 2009). Different sensors and approaches can be used for image collection and processing. The most common technique is to capture photos of a muckpile from fixed ground locations, using a monocular camera and physical scale objects to estimate the scale. This method typically involves a technician walking to the location of a muckpile, placing scale objects in the area of interest, and capturing individual photos. Among the limitations of this technique, discussed by Sanchidrián et al. (2009), the imaging system resolution and image segmentation are of high importance, as both can lead to inaccurate rock



(a) UAV collecting data during a flight mission.



(b) Sieving rock pile material.

**Figure 1:** a) Photo taken during data collection using a UAV system and b) setup for screening rock piles at McEwen Mining’s El Gallo mine.

**Table 1:** UAV specifications provided by DJI (2018a).

Parameter	Specification
Dimensions	1668 mm × 1518 mm × 727 mm
Weight with batteries (no camera)	9.5 kg
Max Takeoff Weight	15.5 kg
Hovering Accuracy	Vertical: ±0.5 m, Horizontal: ±1.5 m
Hovering Time with batteries (no camera)	32 min

**Table 2:** Camera specifications provided by DJI (2018b).

Parameter	Specification
Dimensions	120 mm × 135 mm × 140 mm
Weight	530 g
Resolution	4608 × 3456
Angle of View	72°
Gimbal Accuracy	±0.02°

size measurement. The system resolution is limited by the sensor hardware used, whereas accurate automated segmentation of rock fragments is still considered a challenging task. Most recently, Ramezani et al. (2017) proposed promising results using Deep Neural Networks as a potential first step to improve automated rock segmentation accuracy.

Application of 3D imaging and analysis methods has eliminated the need for placement of scale objects and has reduced the error that can be created by the uneven shape of the rock pile surface. In the work by Onederra et al. (2015), a LiDAR scanner was used to measure fragmentation of a muckpile in an open pit mine. This method improved automated rock segmentation and enabled measurement in poor lighting conditions in underground mines, as shown in Campbell & Thurley (2017). Stereo imaging can also help improve automated rock segmentation as shown in Noy (2012) where the sensor is mounted on a shovel to collect fragmentation data. While the 3D techniques improve image analysis methods, there are still some limiting aspects. One example of this is the significant amount of time that is required to capture detailed scans with LiDAR technology. Another drawback of the current 3D imaging techniques is that they have been limited to capturing images from fixed locations because motion blur can significantly distort the 3D data, making delineation difficult as mentioned in Campbell & Thurley (2017).

In recent years, UAV technology has advanced rapidly. The technology is routinely used in many mining operations for aerial surveying and volume calculation. An example of using UAVs to measure fragmentation of muckpiles in a quarry using photographic methods is given by Tamir et al. (2017). However, in this study, no evaluation of the accuracy

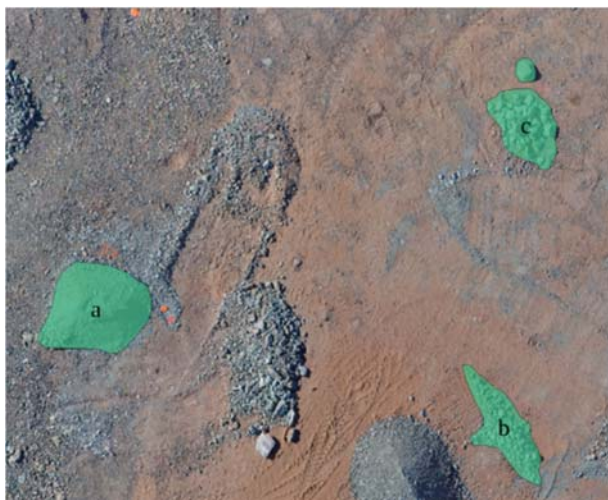
of the collected data and estimated results was provided.

### 3 EQUIPMENT AND METHODOLOGY

In this study, to collect fragmentation data, a test campaign was conducted at McEwen Mining's El Gallo gold mine located in Sinaloa State, Mexico. This campaign was carried out during December 2017. The following sections provide details of the equipment used and the data collection methodology of the campaign.

#### 3.1 UAV System

A commercially available UAV and gimbal camera combination, the DJI Matrice 600 Pro UAV and DJI Zenmuse X5 camera, was used during the test campaign. Figure 1a shows the UAV system capturing photos during a flight mission. The UAV was selected because of its high payload capacity. It could also be used to carry a LiDAR system. During the test campaign a LiDAR system was also used to collect fragmentation data. Results of processing the data collected with the LiDAR system will be presented in future work. Table 1 lists the main specifications of the UAV. The camera was selected because of its high resolution. It was easily integrated with the selected UAV and its gimbal provides physical photo stabilization. Table 2 lists the main specifications of the gimbal camera system. In these tests, flight missions were designed and then the UAV was autonomously flown to capture photographs of muckpiles for analysis. The flight missions used are described in Section 3.3. During the test campaign, fragmentation measurement was run off-line. In fu-



(a) Before ore mixing. Note that the pile between a and b was not used to construct pile d.



(b) After ore mixing.

**Figure 2:** Orthophotos of screening area before and after ore rock piles are mixed. Piles are outlined and labelled.

ture test campaigns, an onboard computer will be used to conduct real-time fragmentation measurement.

### 3.2 Screening of Piles

Rock piles were constructed with sieved rock fragments of different sizes for ore and waste material types. Two screen sizes were used to sieve rock fragments, creating three piles for each material type. These square opening screens had 10.16 cm (4 inches) and 20.32 cm (8 inches) aperture widths. Figure 1b shows the sieving process. This method produced piles with the following fragment size ranges: less than 10.16 cm (pile a in Figure 2a), 10.16 cm – 20.32 cm (pile b in Figure 2a), and greater than 20.32 cm (pile c in Figure 2a). Once Flight Mission A (Section 3.3) was completed to measure the fragmentation of the sieved piles, the sieved piles of the ore material were mixed. This was done so that the accuracy of fragmentation measurement using image analysis could be calculated using a wide range of fragments sizes. Figure 2a illustrates the sieved ore piles before mixing. The mixing was done by the backhoe shown in Figure 1b so that the material was homogenized. Ideally, the piles would have been constructed and mixed on a concrete surface to avoid contamination, however, this was not available at the mine site. Due to this, some rock fragments that were not the sieved size were visible in the pile area. For example, some rock fragments with sizes <10.13 cm were visible in the edge of the >20.26 cm sieved pile. These additional rock fragments were manually masked after identi-

fying outliers. This process reduced the errors in the minimum rock fragment size measured for the piles since outliers were removed. The mixed pile’s fragmentation size was then measured by the UAV using Flight Mission B. Figure 2b shows the mixed pile (pile d) that was built from mixing piles a, b and c in Figure 2a.

### 3.3 Flight Missions

Flight missions were created and flown using the DJI Ground Station Pro application. This application allows the user to specify an area for 3D mapping and to specify mission parameters such as altitude or GSR, overlap, and flight speed. This application determines the mission waypoints for 3D mapping using the specified camera parameters including focal length and resolution. The flight missions flown, their parameters, and target piles during the test campaign are provided in Table 3. All flights were flown with the gimbal pitch angle stabilized at 90° down. Flight Mission A was flown over the whole screening area at a flight altitude of 20 m. This flight was used to measure the volume and pre-mixed rock size distribution of the ore sieved piles. It was also used to measure the rock fragmentation of the waste sieved piles. Figure 3 illustrates Flight Mission A (light blue) over the area where the sieved piles were constructed. Flight Mission B was flown over the mixed ore pile at an altitude of 15 m to measure its volume and rock fragmentation. Flight Mission C was flown over the waste sieved piles at an altitude of 15 m to increase GSR for comparison with the rock fragmentation measured for these piles in Flight

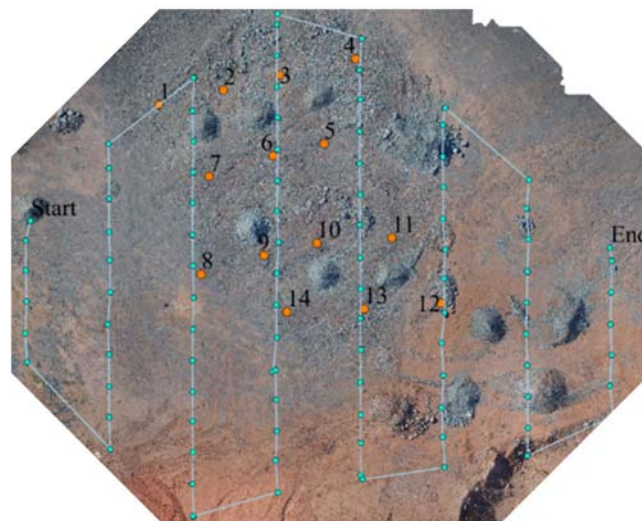


**Figure 3:** Flight Mission A (light blue) and numbered GCPs (orange) plotted on an orthophoto of screening area.

**Table 3:** Flight missions used to collect data.

Flight Mission	Target Piles	Cover Area	Flight Time	Number of Photos	Altitude	GSR (pixels/m)	Front Overlap	Side Overlap
A	Sieved ore and waste	0.27 ha	4 min 49 sec	97	20 m	200	80%	60%
B	Mixed ore	0.05 ha	2 min 45 sec	64	15 m	250	90%	60%
C	Sieved waste	0.05 ha	2 min 26 sec	56	15 m	250	90%	60%

Mission A. Fourteen (14) Ground Control Points (GCPs) were marked on the ground and measured throughout the area using a total station so that the accuracy of the 3D model generated could be calculated. The marks on the ground should be visible to the camera when the UAV is in flight. Figure 3 shows the GCPs (orange) plotted throughout the sieving area.

## 4 DATA PROCESSING AND RESULTS

### 4.1 3D Model Generation and Accuracy

To use image analysis for measuring rock fragmentation, an image scale or set of images scales are required to calculate particle sizes. A 3D model of the pile was generated from the images captured by the UAV. Onboard GPS and camera orientation measurements from the UAV were used to compute image scale without using physical scaling objects on the muckpile. The process used to compute image scale is described in Section 4.2. To create the 3D model from photos captured using the UAV, OpenDroneMap (2018), an open source software, was used. This software takes a set of images and their GPS locations and processes them to generate a 3D model of the area captured by the image set. This 3D model includes geographic data such as point clouds, meshes, digital terrain models, digital surface models, and orthophotos.

Geographic data for each flight mission, described in Section 3.3, was generated using OpenDroneMap. The image scale calculation in this paper used the point cloud generated; however, a digital terrain model or digital surface model could also be used. To georeference geographic data, the GPS data logged by the UAV or GCPs and their location in the set of images can be used. Placing and maintain-

ing a set of GCPs on an active muckpile is laborious, logistically complex, and may not be feasible. Therefore, the GPS data recorded by the UAV was used in georeferencing the 3D model even though GCPs were available in this study. This GPS data is recorded in each photo's file during flight and OpenDroneMap automatically reads and uses this data for georeferencing.

To evaluate the accuracy of the 3D models generated, the agreement between the generated 3D model and a reference model is evaluated. Since the image scale calculation involves a 3D distance between points, distances between GCPs are considered as an appropriate model to assess the accuracy of the 3D model. This has assumed that the GCPs are correct because they have been recorded with a more precise total station. The GPS data recorded by the UAV is subject to a  $\pm 1.5$  m horizontal and  $\pm 0.5$  m vertical hovering accuracy so it is considered less precise than the GCPs. The assessment of accuracy is done by calculating the Root Mean Square Error (RMSE), a key statistic used to determine remote sensing accuracies (Congalton 2016). Equation 1 has been adapted to calculate 3D RMSE.

$$RMSE = \sqrt{\frac{\sum_i^n (e_i)^2}{n}} \quad (1)$$

where

$$(e_i)^2 = (x_{ri} - x_{mi})^2 + (y_{ri} - y_{mi})^2 + (z_{ri} - z_{mi})^2$$

With  $x_{ri}$ ,  $y_{ri}$  and  $z_{ri}$  are the components of the reference model's distance between GCPs in the x, y, and z directions, respectively. The distance components of the generated 3D model between GCPs in the x, y, and z directions are  $x_{mi}$ ,  $y_{mi}$  and  $z_{mi}$ , respectively. The number of samples is represented by  $n$ . Table 4 provides an example of the generate

**Table 4:** 3D distance error between GCPs for 3D model created using images captured during Flight Mission A. Values in meters.

	1	2	3	4	5	6	7	8	9	10	11	12	13	14
1	0.000	0.008	-0.010	-0.207	-0.169	-0.188	-0.268	-0.408	-0.468	-0.398	-0.543	-0.377	-0.519	-0.478
2		0.000	-0.017	-0.215	-0.197	-0.279	-0.311	-0.396	-0.469	-0.419	-0.564	-0.359	-0.501	-0.452
3			0.000	-0.195	-0.137	-0.227	-0.225	-0.320	-0.364	-0.335	-0.490	-0.262	-0.394	-0.344
4				0.000	-0.184	-0.323	-0.369	-0.446	-0.426	-0.373	-0.449	-0.206	-0.376	-0.387
5					0.000	-0.090	-0.171	-0.255	-0.232	-0.206	-0.354	-0.127	-0.252	-0.213
6						0.000	-0.075	-0.120	-0.138	-0.123	-0.325	-0.114	-0.205	-0.121
7							0.000	-0.084	-0.197	-0.192	-0.391	-0.218	-0.300	-0.191
8								0.000	-0.128	-0.176	-0.350	-0.281	-0.321	-0.200
9									0.000	-0.042	-0.214	-0.086	-0.129	0.011
10										0.000	-0.181	-0.035	-0.088	-0.009
11											0.000	0.227	0.042	-0.105
12												0.000	0.010	-0.104
13													0.000	-0.118
14														0.000

**Table 5:** RMSEs for flight missions.

Flight Mission	Number of Points (n)	3D RMSE
A	14	0.287 m
B	11	0.177 m
C	7	0.114 m

model's 3D distance error ( $e_i$ ) created for fourteen GCPs using the image set collected during Flight Mission A. Table 5 gives the 3D RMSEs calculated for each flight mission. It is observed that for flight missions with a lower altitude (Flight Mission B and C) a lower RMSE was found, indicating higher accuracy. The magnitude of RMSEs relative to the altitude of flight missions is similar to the results reported by Bamford et al. (2017c) during previous laboratory-scale tests. Future work will investigate whether the accuracy of the 3D model can be improved when GCPs are used for georeferencing instead of GPS data.

#### 4.2 Image Scale Estimation

An emerging approach to conduct rock fragmen-

tation measurement is by using an orthophoto created using geographic data processing software, such as OpenDroneMap,. This method estimated image scale by assuming that the GSR of the orthophoto is accurate. The work by Tamir et al. (2017) uses an orthophoto for fragmentation measurement. An orthophoto has a fixed GSR which can be directly used as image scale in image analysis software. While this is convenient, orthophoto files tend to be large and demanding on computing resources and are produced at low resolution by default. They also include large, unpredictably shaped areas that should not be measured for fragmentation analysis. An example of this is an inclusion of the pit floor and highwall because the flight mission covered the area outside the muckpile. These properties indicate that using orthophotos for measuring fragmentation will be diffi-

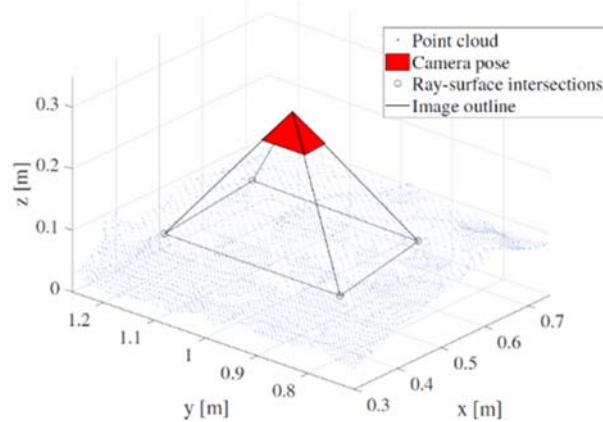


**Figure 4:** Schematic of method used to estimate image scale using 3D model and UAV sensor data, Bamford et al. (2017a).

**Table 6:** Image scales and their errors estimated for images used to measure fragmentation of sieved and mixed ore piles.

Flight Mission	Altitude	Pile Description	Image Scale along top edge of photo	Error range along top edge of photo	Image Scale along bottom edge of photo	Error range along bottom edge of photo
A	20 m	Sizes greater than 20.32 cm	209.79 pixels/m	-2.78 to +2.71	209.79 pixels/m	-2.78 to +2.71
A	20 m	Sizes from 10.16 cm to 20.32 cm	209.51 pixels/m	-2.77 to +2.70	210.06 pixels/m	-2.78 to +2.71
A	20 m	Sizes less than 10.16 cm	210.60 pixels/m	-2.80 to +2.73	211.15 pixels/m	-2.81 to +2.74
B	15 m	Mixed pile	264.69 pixels/m	-2.72 to +2.66	265.39 pixels/m	-2.73 to +2.68

**Table 7:** Image scales estimated and their errors for images used to measure fragmentation of sieved waste piles.

Flight Mission	Altitude	Pile Description	Image Scale along top edge of photo	Error range along top edge of photo	Image Scale along bottom edge of photo	Error range along bottom edge of photo
A	20 m	Sizes greater than 20.32 cm	211.69 pixels/m	-2.83 to +2.75	212.25 pixels/m	-2.84 to +2.77
A	20 m	Sizes from 10.16 cm to 20.32 cm	209.51 pixels/m	-2.77 to +2.70	210.06 pixels/m	-2.78 to +2.71
A	20 m	Sizes less than 10.16 cm	211.69 pixels/m	-2.83 to +2.75	212.25 pixels/m	-2.84 to +2.77
C	15 m	Sizes greater than 20.32 cm	260.88 pixels/m	-1.69 to +1.67	261.56 pixels/m	-1.70 to +1.68
C	15 m	Sizes from 10.16 cm to 20.32 cm	262.56 pixels/m	-1.72 to +1.69	263.25 pixels/m	-1.73 to +1.70
C	15 m	Sizes less than 10.16 cm	259.22 pixels/m	-1.67 to +1.65	259.90 pixels/m	-1.68 to +1.66

cult to automate. Due to these limitations, we have chosen to use individual images to measure fragmentation.

Using image analysis with individual images requires an image scale to be estimated. If there are no physical scales in the area captured by the photo, then image scale must be estimated. A simple trigonometric model relying on camera field of view and flight altitude can be used to estimate image scale. However, a 90° gimbal pitch angle and flat surface must be assumed. Equation 2 provides the image scale along the top and bottom edges of a photo calculated using this simple model.

$$\text{image scale} = \frac{i_w}{2z \tan(f_h/2)} \quad (2)$$

Where  $z$  is the flight altitude above flat surface,  $f_h$  is the camera's horizontal field of view, and  $i_w$  is the image width in pixels. From our experience, when the UAV is used to measure fragmentation for a pile against a mine's highwall, then the pilot will typically change the gimbal pitch angle so that a safe distance is always maintained from the highwall. Changing the gimbal pitch angle invalidates the gimbal pitch angle assumption in the simple model, making the image scale equation much more complex. To avoid using physical scaling objects and assuming the simple model, the 3D surface model, onboard sensor data recorded by the UAV, and camera parameters were used together to estimate image scales. A schematic of the method used to estimate image scale using the 3D model and UAV sensor data is given in Figure 4. The process used to estimate image scale is described in detail in Bamford et al. (2017a) and is presented at the end of this paper in Appendix A.

To estimate error in the calculated image scales, the 3D RMSE for the 3D models (discussed in Section 4.1) was used. Equation 3 calculates the image scale error using the 3D RMSE.

$$\text{scale error} = \text{scale} - \frac{i_w}{i_w/(\text{scale}) \pm \text{RMSE}} \quad (3)$$

Where  $i_w$  is the image width in pixels, scale is the estimated image scale using the method described in Appendix A, and RMSE is the 3D RMSE. Table 6 and Table 7 present the image scale and image scale error for each photo used to measure fragmentation for ore and waste piles, respectively. Since the image analysis software only accepts an image scale along the top and bottom edge of the photo, the image scale is estimated along the top and bottom edges. There is approximately a 10 pixels/m increase between the flight mission GSRs in Table 3 and the estimated image scales in Table 6 and Table 7. For example, Flight Mission A has a GSR of 200 pixels/m and the image scale estimated for the pile with sizes greater than 20.32 cm during Flight Mission A was 209.79 pixels/m along the top and bottom edge of the image. This increase is caused by a difference between the planned flight mission altitude and the altitude measured above the 3D model. One example of this difference is that the altitude for Flight Mission A is 20 m, and the altitude measured above the 3D model for the photo captured at the end of the mission is 18.51 m. The differences in altitudes are expected to be due to (1) the assumption in flight mission planning that the surface is flat, and (2) the added vertical distance between the camera and the GPS sensor. For the UAV system described in Section 3.1, the vertical distance is 40 cm.

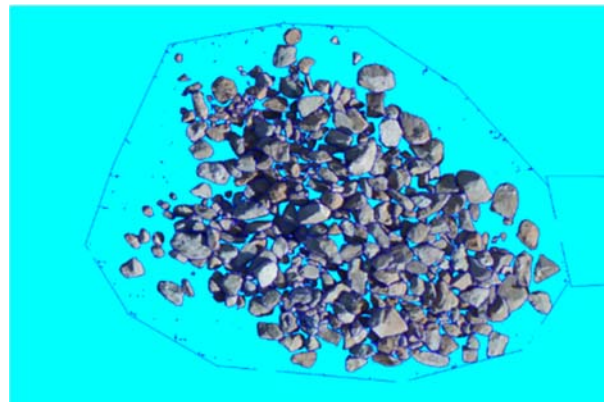
#### 4.3 Fragmentation Measurement of Mixed Pile

To evaluate the accuracy of fragmentation measurement of the ore mixed pile, the rock size distributions using the image analysis method and sieving are compared.

For image analysis Split-Desktop by Split Engineering LLC. (2018) was used. This software takes a



(a) Image collected by UAV.



(b) Delineated image.

**Figure 5:** Image analysis of waste rock pile with rock fragment sizes between 10.16 cm and 20.32 cm using photo captured during Flight Mission C. In 5b, blue regions represent rock fragment boundaries and light blue regions are masked.

photograph and delineates rock fragments using image segmentation. Figure 5 illustrates the delineation of rock fragments using image segmentation for one of the waste rock piles (10.16 to 20.32 cm). To measure the rock sizes, estimated image scales are manually input into the software. Manual editing was used to improve the rock delineation process. In future work, custom image segmentation algorithms will be implemented to eliminate the manual editing step and to help automate fragmentation measurement. Figure 6 and Table 9 show the measured fragmentation produced by image analysis for the mixed ore rock pile.

To determine the sieving size distribution of the mixed pile, volumes were calculated for each sieved pile. This was done by computing the volume between a digital surface model and a digital terrain model of each pile generated using OpenDroneMap at a resolution of 10 pixels per meter. To compute the volume between the two models for each pile, the outlines of each pile in Figure 3 were used. This

resulted in the volumes reported in Table 8. The volume measured for the mixed pile is 0.41 m<sup>3</sup> greater than for the combination of the sieved piles. This difference is thought to be caused by an accumulation of small variations in the digital terrain model underneath the piles. Ideally, the bottom surface should have been measured before placement of the piles to ensure more accurate volume measurement. Figure 6 plots the sieving size distribution calculated for the mixed ore pile using the volumes in Table 8. As can be seen in Figure 6, the residuals between the image analysis and sieve analysis are 7.96% and 0.82% for the sieve sizes of 10.16 cm and 20.64 cm, respectively (less than 10% passing). This range is considered acceptable because these residuals are expected to be caused by the effect of particle shape and particle occlusion, known limitations of image analysis. The larger residuals found for the lower sieve size (10.16 cm) is caused by a lesser proportion of the fines material being visible on the surface because it was mixed in from the bottom of

**Table 8:** Volumes calculated for sieved and mixed ore rock piles labeled in Figure 2.

Pile Label	Description	Volume
a	Sizes greater than 20.32 cm	0.51 m <sup>3</sup>
b	Sizes from 10.16 cm to 20.32 cm	0.64 m <sup>3</sup>
c	Sizes less than 10.16 cm	3.45 m <sup>3</sup>
a + b + c	Sieved piles	4.60 m <sup>3</sup>
d	Mixed pile	5.01 m <sup>3</sup>

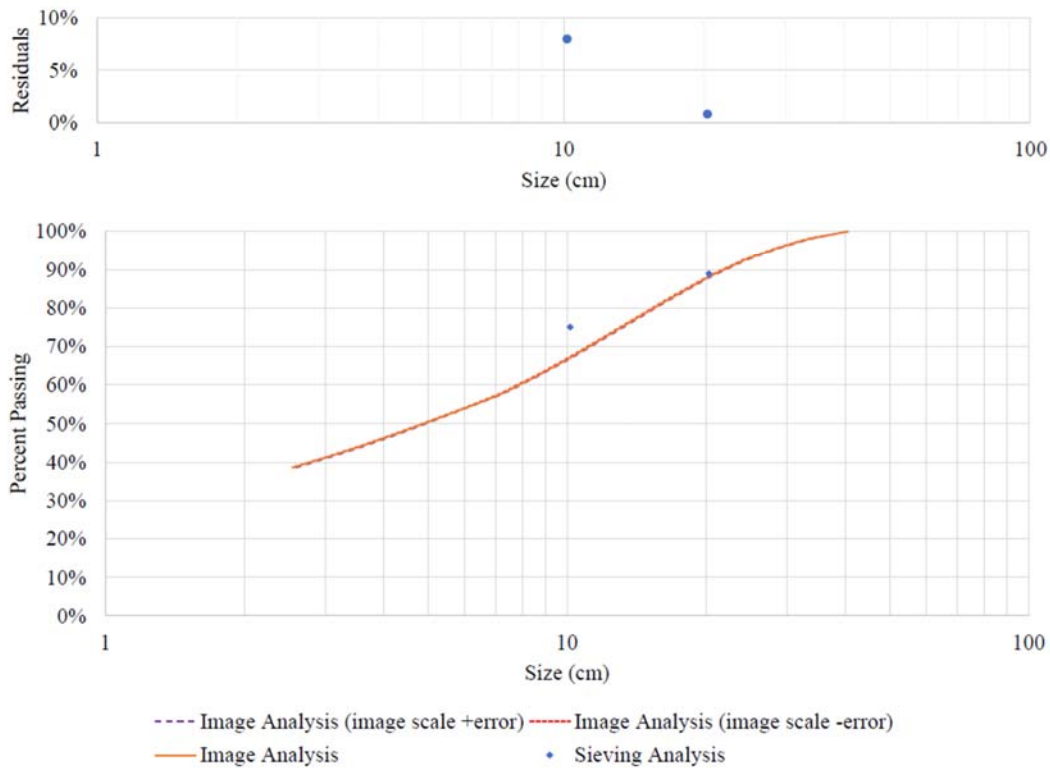


**Figure 6:** Rock size distributions of mixed ore rock pile measured using sieving and image analysis. Rock size distributions are plotted to show variation caused by image scale error. This variation is small and is close to the image analysis distribution.

**Table 9:** Summary of image analysis measurements shown in Figure 6.

Pile Description	$P_{20}$ (cm)	$P_{50}$ (cm)	$P_{80}$ (cm)	$P_{max}$ (cm)
Mixed pile	0.49	4.89	15.43	39.30



the pile. Most of the finer material was at the bottom of the pile because the mixed pile (d) was built on top of the smaller than 10.16 cm sieved pile (a), as shown in Figure 2. To understand this error better, a series of mixing the pile and measuring the fragmentation should be conducted to see if the sieved rock size distribution will result by averaging or combining the surface size distributions. This concept could also be applied to an operating mine, where continuous measurement of the rock size distribution could be done during excavation to obtain a better prediction of fines. This is because most fines end up in the bottom of the muckpile due to segregation and they are exposed during excavation.

#### 4.4 Influence of UAV Flight Altitude on the Fragmentation Measurement

To understand the impact of GSR on the minimum detectable fragment size and rock size distribution accuracy, image analysis was conducted on each of the sieved waste piles to measure fragmentation for two different flight altitudes (20 m and 15 m). The rock size distributions are then compared to each other and the expected size ranges created by sieving.

Each flight altitude produces a different GSR as

shown in Table 3 and the estimated image scales in Table 7. Since we have one closed rock size range between 10.16 cm to 20.32 cm, we can calculate a GSR that will allow rocks in this range to be reliably delineated. In Split-Desktop, particles smaller than 16 square pixels can not be reliably automatically delineated. Assuming the 10.16 cm size rocks do not pass through the square screen apertures, this would require the condition on GSR given in Equation 4.

$$\begin{aligned} \text{GSR} &> \frac{16 \text{ pixels}^2}{(10.16)^2 \text{ cm}^2} = \frac{16 \text{ pixels}^2}{0.0103226 \text{ m}^2} \\ &= 1550 \frac{\text{pixels}^2}{\text{m}^2} = 39 \frac{\text{pixels}}{\text{m}} \end{aligned} \quad (4)$$

Therefore, to reliably delineate rocks that are 10.16 cm and larger, a GSR of 39 pixels per meter or greater is required. For both flight altitudes, the GSR is greater than this value (250 pixels per meter for 15 m flight altitude, and 200 pixels per meter for 20 m flight altitude). Thus, the image analysis is able to reliably delineate the target rock fragment sizes. Figure 7 and Table 10 show the waste rock size distributions produced by image analysis for Flight Mission A and C (20 m and 15 m flight altitudes, respectively). Table 10 illustrates that the range of measured sizes within the sieving size range was only 61.1% and 60.9% for the middle size range piles

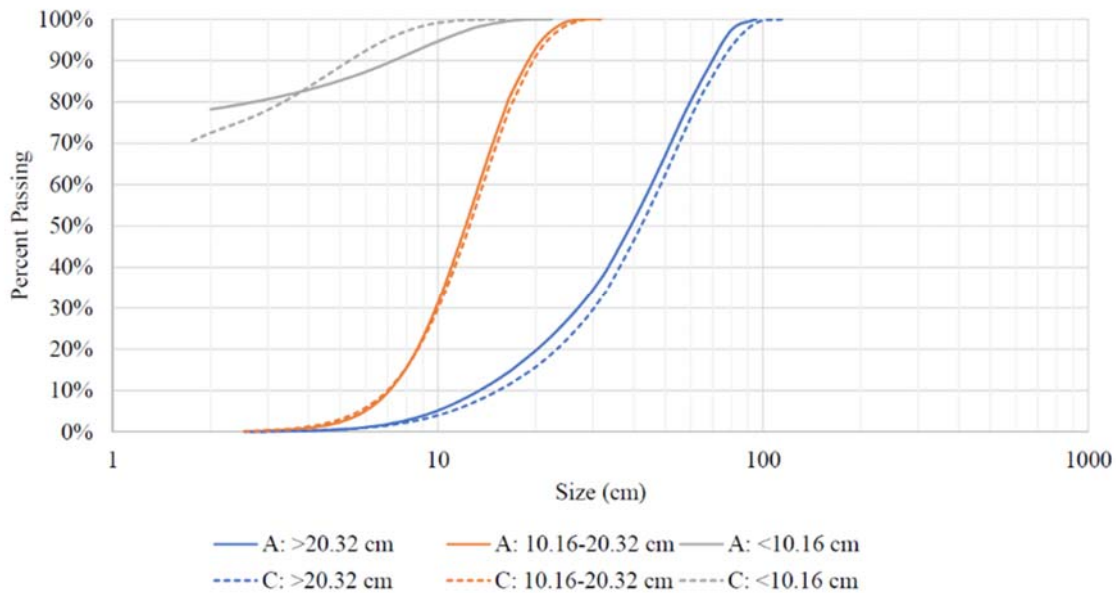


**Figure 7:** Rock size distributions of waste rock piles measured using image analysis at resolutions of 200 pixels/m (Flight Mission A) and 250 pixels/m (Flight Mission C).

**Table 10:** Summary of image analysis measurements shown in Figure 7.

Flight Mission	Altitude	Pile Description	$P_{20}$ (cm)	$P_{50}$ (cm)	$P_{80}$ (cm)	$P_{\max}$ (cm)	Percent within sieved range
A	20 m	Sizes greater than 20.32 cm	20.20	39.27	59.79	88.39	79.83%
A	20 m	Sizes from 10.16 cm to 20.32 cm	8.63	12.17	16.44	28.22	61.16%
A	20 m	Sizes less than 10.16 cm	0.01	0.02	2.73	18.87	94.86%
C	15 m	Sizes greater than 20.32 cm	23.25	42.08	63.19	97.94	83.86%
C	15 m	Sizes from 10.16 cm to 20.32 cm	8.68	12.49	16.99	27.21	60.88%
C	15 m	Sizes less than 10.16 cm	0.02	0.33	3.35	14.63	99.21%

in Flight Mission A and C, respectively. This relatively high error is discussed in Section 5. For the other piles, the range of particle sizes that are measured within the correct sieving sizes, ranges from 79.8% to 99.2%, which is considered acceptable.

As can be seen in Figure 7, the coarse size sieved piles ( $>10.16$  cm) are not as affected by the flight altitude as the pile of fine material ( $<10.16$  cm). This difference is caused by the lower GSR at the higher flight altitude chosen for Flight Mission A. The low GSR, in turn, makes a larger amount of smaller rock fragments non-detectable during image analysis. This can be seen in Figure 7 for the pile with sizes less than 10.16 cm for the two flight altitudes. At 20 m altitude (Flight Mission A), the minimum detectable size was 2 cm with 78.2% below this size. At 15 m altitude (Flight Mission B), the minimum detectable size was 1.7 cm with 70.1%. This decrease in percent passing at a higher GSR indicates that more rock fragments are detected and measured at the 15 m altitude than at the 20 m altitude.

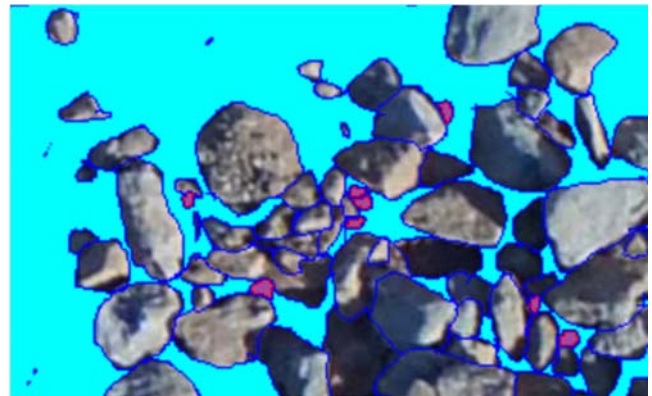
Since a high GSR is desirable to detect more fine material, a low flight altitude will be required. However, there are a number of factors that will impact the selection of flight altitude. This includes the size of the area that has to be covered and the time available since a low altitude will require more scanlines, and time, to cover the area. Another consideration includes the number of photos that are accepted by the geographic data processing software, since a lower altitude will produce more photos to process. From experience, caution must be taken when flying at low altitudes because the risk of collision is much higher. This is due to weak GPS signal in the lower benches of an open pit mine and also because the airspace near a muckpile at lower altitudes is frequently occupied by tall mining equipment, such as drilling rigs.

## 5 DISCUSSION

This section discusses some of the sources of error during rock size distribution measurement and the possible solutions that will be explored in future work. Relatively large errors were found when measuring the fragmentation of the medium size range (10.16 cm to 20.32 cm) waste material (Figure 7). This includes 30% of material smaller than 10.16 cm and 10% of material larger than 20.32 cm. While the 10% of oversize material is considered acceptable, the 30% error is considered large (Sanchidrián et al. 2009). This error is expected to be caused by particle over-segmentation, occlusion and shape. For example, Figure 8 illustrates particle occlusion for the medium range waste pile for Flight Mission C. In Figure 8, there are a number of particles that are measured as a smaller size than their sieved size because they are overlapped by other particles. A possible solution to this limitation is to use a 3D model to predict whether a particle is overlapped or not (Onederra et al. 2015, Campbell & Thurley 2017). In future work, this technique will be applied to LiDAR data collected during the test campaign and the 3D model generated using the 2D images. Another potential source of error is caused by over-segmentation. This error could be mitigated with more manual editing, however, since the goal of UAV measurement of rock fragmentation should be to automate data collection and processing, this is not feasible. To help improve the accuracy of segmentation, the use of Deep Neural Networks for rock segmentation shows promise and will be investigated in future work. As mentioned in Section 4.3, mixing the pile to expose different surface configurations may also decrease the error caused by particle shape when combining a series of measurements.



(a) Raw image collected by UAV.



(b) Delineated image with overlapped rocks highlight purple.

**Figure 8:** Close up of image analysis of waste rock pile with rock fragment sizes between 10.16 cm and 20.32 cm using photo captured during Flight Mission C. In 8b, blue regions represent rock fragment boundaries, purple regions represent overlapped rocks that are measured as less than 10.16 cm, and light blue regions are masked.

## 6 CONCLUSION

This paper evaluated the quality of photographic data collected by UAVs for measuring fragmentation of muckpiles. The UAV system used to measure rock piles for fragmentation analysis was described along with the data collection methods. Using rock piles that were constructed with sieved rock fragments of different sizes and material types, the accuracy of each step was evaluated. The accuracy of the 3D model generated by the UAV was evaluated using the RMSE statistic computed by using the distance between reference GCPs. This resulted in an RMSE ranging from 0.11 m to 0.29 m for the data processed in the test campaign. To decrease this error it was suggested to include GCPs during 3D model generation. The computed image scale was then evaluated by estimating the error propagated by the 3D model. This resulted in very small error, in the range of  $\pm 2.8$  pixels/m. This error is expected to decrease with increased 3D model accuracy. The measured rock size distribution for a mixed pile constructed from sieved piles was comparable with sieving analysis with a maximum error of 7.96%. This error is possibly caused by particle shape and occlusion as well as the limitation of image analysis using surface measurement to represent volume.

The paper also investigated the impact of flight altitude on the measured rock size distribution. The effect of flight altitude was shown to have a larger impact on the minimum size that is detectable. This effect was shown to largely impact the measurement of fine material, with smaller impact on the measurement of coarser material. Flight altitude, and a high GSR, has been shown to improve the particle segmentation process through decreasing the minimum detectable size.

## ACKNOWLEDGEMENTS

This work was supported by McEwen Mining, Split-Engineering, the University of Toronto's Dean's Strategic Fund, the Canada Foundation for Innovation John R. Evans Leaders Fund, and the Natural Sciences and Engineering Research Council of Canada.

## REFERENCES

- Bamford, T., Esmaili, K. and Schoellig, A. P. (2017a) "Point-cloud-based aerial fragmentation analysis for application in the minerals industry", Technical Report, arXiv. Available from: <https://arxiv.org/abs/1703.01945>
- Bamford, T., Esmaili, K. and Schoellig, A. P. (2017b) "A real-time analysis of post-blast rock fragmentation using UAV technology", International Journal of Mining, Reclamation and Environment, Vol 31, No. 6, pp 439–456.
- Bamford, T., Esmaili, K. and Schoellig, A. P. (2017c) "Point-cloud-based aerial fragmentation analysis for application in the minerals and aggregates industries", IEEE International Conference on Intelligent Robots and Systems, Poster.
- Campbell, A. D. and Thurley, M. J. (2017) "Application of laser scanning to measure fragmentation in underground mines", Mining Technology, Vol 126, No. 4, pp 240–247.
- Congalton, R. G. (2016) "Assessing positional and thematic accuracies of maps generated from remotely sensed data", in P. S. Thenkabail, ed., Remote Sensing Handbook, Vol 1, CRC Press.
- DJI (2018a) "Matrice 600 pro: Simply professional performance". Available from: <https://www.dji.com/matrice600-pro>
- DJI (2018b) "Zenmuse x5: Aerial imaging evolved". Available from: <https://www.dji.com/zenmuse-x5>
- Kanchibotla, S. S., Valery, W. and Morrell, S. (1999) "Modelling fines in blast fragmentation and its impact on crushing and grinding", Explo '99—A conference on rock breaking, The Australasian Institute of Mining and Metallurgy, Kalgoorlie, Australia, pp 137–144.
- McKee, D. J. (2013) "Understanding Mine to Mill", CRC ORE.
- Mosher, J. (2011) "Crushing, milling, and grinding", in P. Darling, ed., Society for Mining, Metallurgy & Exploration (SME) Mining Engineering Handbook, 3rd edn., Vol. 2, SME, Chapter 14.2, pp 1461–1465.
- Noy, M. J. (2012) "Automated rock fragmentation measurement with close range digital photogrammetry", in Measurement and Analysis of Blast Fragmentation, CRC Press.
- Onederra, I., Thurley, M. J. and Catalan, A. (2015) "Measuring blast fragmentation at Esperanza mine using high-resolution 3d laser scanning", Mining Technology, Vol 124, No. 1, pp 34–36.
- OpenDroneMap (2018) "OpenDroneMap: Open source toolkit for processing aerial drone imagery". Available from: <http://opendronemap.org/>
- Ramezani, M., Nouranian, S., Bell, I., Sameti, B. and Tafazoli, S. (2017) "Fast rock segmentation using artificial intelligence to approach human-level accuracy", Journal of Explosives Engineering, Vol 34, No. 4, pp 28–32.
- Sanchidrián, J. A., Segarra, P., Ouchterlony, F. and López, L. M. (2009) "On the accuracy of fragment size measurement by image analysis in combination with some distribution functions", Rock Mechanics and Rock Engineering, Vol 42, No. 1, pp 95–116.
- Split Engineering LLC. (2018) "Split-desktop: Fragmentation analysis software". Available from: <https://www.spliteng.com/products/split-desktop-software/>

Tamir, R., Wagner, M., Campbell, J. and Dakers, N. (2017) “Utilization of aerial drones to optimize blast and stockpile fragmentation”, *Journal of Explosives Engineering*, Vol 34, No. 4, pp 6–15.

## APPENDIX A

This appendix describes a point-cloud-based method used to calculate image scale. The proposed method uses a monocular camera attached to a UAV, onboard sensors to measure UAV and camera orientation, and global position information (e.g., GPS or an external motion capture system) to measure camera position.

### A.1 3D Model Creation

The first step in this process is creating a 3D model, or point cloud. The UAV is used to take overlapping images around the area of interest. For example, if the area of interest is a soccer field, the UAV will fly parallel scanlines up and down the field capturing photos at a fixed spacing.

Next, a geographic data processing software, such as OpenDroneMap, is used for 3D model reconstruction. First, the software takes a set of images, detects and describes features in them, and then matches these features between images. With these known matches, bundle adjustment is conducted to create a 3D reconstruction of the scene. The 3D model is then transformed, or georeferenced, using the GPS data captured for each image. The 3D model created in this step can be used, or taken from, other analysis projects, such as drill and blast campaigns or topographic surveys.

### A.2 Camera Intrinsic Parameters

The next step towards obtaining image scale for photographic fragmentation analysis is the measurement of camera intrinsic parameters. Camera intrinsic parameters are innate characteristics of the camera and sensor, and can be measured using camera calibration software. For this paper, an open source camera calibration package was used. These parameters are required to transform a point, represented by pixel coordinates, in the image to a point on the image in the GPS frame (world frame). Once they are estimated, the camera parameters are stored in a matrix defined in Equation A1.

$$\mathbf{K} = \begin{bmatrix} f_x & s & c_x \\ 0 & f_y & c_y \\ 0 & 0 & 1 \end{bmatrix} \quad (\text{A1})$$

Where  $f_x$  and  $f_y$  are focal lengths in the sensor’s x- and y-direction, respectively.  $c_x$  and  $c_y$  are pixels coordinates of the optical center.  $s$  is the skew between sensor axes.

### A.3 Camera Extrinsic Parameters

The position and orientation of the camera in the world frame is required as an origin of the ray that will project image points onto the 3D model. The position and orientation is combined into the transformation matrix of the camera. Equation A2 defines the structure of the camera transformation matrix.

$$\mathbf{T} = \begin{bmatrix} \mathbf{C} & \mathbf{r} \\ \mathbf{0}^T & 1 \end{bmatrix} \quad (\text{A2})$$

Where  $\mathbf{T}$  is referred to as the  $(4 \times 4)$  transformation matrix of the camera with respect to the world frame origin.  $\mathbf{C}$  is a  $(3 \times 3)$  rotation matrix in the special orthogonal group,  $SO(3)$ , that represents the camera’s orientation relative to the world frame.  $\mathbf{r} = (x_r, y_r, z_r)$  is a translation vector that represents the camera’s position in the world frame. The transformation matrix is also known as the camera extrinsic parameters, and comprises a minimum of six parameters to describe position and orientation in the special Euclidean group,  $SE(3)$ . For this method, the camera position and orientation is estimated from onboard sensor measurement of camera orientation and UAV position and orientation.

### A.4 Ray Equation

This section derives an equation to represent a ray from pixel coordinates in the image to the world frame using the camera parameter matrix defined in Equation A1 and the camera transformation matrix defined in Equation A2. This derived equation is used to represent each ray projected from the four corners of the image so that the rays can be intersected with the 3D model. A pixel location in the image,  $\mathbf{p}$ , is represented by coordinates  $u$  and  $v$ , where  $u$  and  $v$  are integers. The pixel location,  $\mathbf{p}$ , is then represented in the image using homogeneous coordinates,  $\tilde{\mathbf{p}} = (u', v', w')$ . The non-homogeneous pixel coordinates are computed using Equation A3.

$$u = \frac{u'}{w'}, v = \frac{v'}{w'} \quad (\text{A3})$$

To represent the point,  $\mathbf{p}$ , in the image as  $\tilde{\mathbf{p}}$ , we set  $w' = 1$  such that the center of the image frame is the origin and points are mapped to the plane  $w' = 1$ . The first step to find an equation to represent a ray from image pixel coordinates to the world frame, is to determine the direction of the ray in the image. The direction of the ray in the image,  $\tilde{\mathbf{p}}_c$ , from the homogeneous pixel location,  $\tilde{\mathbf{p}}$ , for a camera with a camera parameter matrix,  $\mathbf{K}$ , is calculated using Equation A4.

$$\tilde{\mathbf{p}}_c = \mathbf{K}^{-1}\tilde{\mathbf{p}} \quad (\text{A4})$$

Using  $\tilde{\mathbf{p}}_c$  from Equation A4, the ray direction in the image is transformed into the world frame. This transformation assumes that camera distortion has been removed from the image to ensure that the ray in the world frame is straight and follows the same

direction as the ray in the image frame. The homogeneous ray direction (a  $(4 \times 1)$  vector) in the world frame,  $\tilde{\mathbf{p}}_m$ , is computed using the ray direction in the image,  $\tilde{\mathbf{p}}_c$ , and the camera transformation matrix, according to Equation A5.

$$\tilde{\mathbf{p}}_m = \mathbf{T} \begin{bmatrix} \tilde{\mathbf{p}}_c \\ 1 \end{bmatrix} \quad (\text{A5})$$

Where  $\tilde{\mathbf{p}}_m = (x_m, y_m, z_m, 1)$ , with  $x_m, y_m, z_m$  representing the slope along each axis in the world frame. Once the ray direction in the world frame,  $\tilde{\mathbf{p}}_m$ , is determined using Equation A5, the equation for the ray in the world frame emitting from the pixel location,  $\mathbf{p}$ , is represented by Equation A6.

$$\tilde{\mathbf{q}} = \begin{bmatrix} \mathbf{r} \\ 1 \end{bmatrix} + \alpha \tilde{\mathbf{p}}_m \quad (\text{A6})$$

Where  $\tilde{\mathbf{q}} = (x, y, z, 1)$  is a homogeneous point on the ray at the position  $\mathbf{r} = (x_r, y_r, z_r)$  in the world frame,  $x, y$  and  $z$  are components in the world frame, and  $\alpha$  is a scalar, since the pixel location is projected along the ray. For example, if Equation A6 is used to represent the ray emitted from a point in the image to a flat surface on a plane at  $z = 0$ , then Equation A6 can be rearranged to solve for  $\alpha$ , as shown in Equation A7.

$$\alpha = -\frac{z_r}{z_m} \quad (\text{A7})$$

### A.5 Plane and Line Parameterization

To find the intersection of the ray with the 3D model, the model is first triangulated so that each triangle is represented as a plane. The three corners of each triangle, represented as  $\mathbf{p}_0, \mathbf{p}_1$  and  $\mathbf{p}_2$ , are used to represent a plane such that a general point on the plane is represented by Equation A8.

$$\mathbf{p}_0 + (\mathbf{p}_1 - \mathbf{p}_0)\eta + (\mathbf{p}_2 - \mathbf{p}_0)\mu \quad (\text{A8})$$

With  $\eta, \mu \in \mathbb{R}$ . Using two points along the ray emitting from a corner pixel, a simple line equation is then created. For example, a point at the position of the camera,  $\mathbf{p}_a = \mathbf{r}$ , and a point intersecting a surface at  $z = 0$ ,  $\mathbf{p}_b$ , both are along the ray. Equation A9 gives the equation of the line along the ray emitting from a corner pixel.

$$\mathbf{p}_a + (\mathbf{p}_b - \mathbf{p}_a)t \quad (\text{A9})$$

With  $t \in \mathbb{R}$ . The line and plane parameters at the point of their intersection can then be solved according to Equation A10.

$$\begin{bmatrix} t \\ \eta \\ \mu \end{bmatrix} = \begin{bmatrix} (x_a - x_b) & (x_1 - x_0) & (x_2 - x_0) \\ (y_a - y_b) & (y_1 - y_0) & (y_2 - y_0) \\ (z_a - z_b) & (z_1 - z_0) & (z_2 - z_0) \end{bmatrix}^{-1} \begin{bmatrix} (x_a - x_0) \\ (y_a - y_0) \\ (z_a - z_0) \end{bmatrix} \quad (\text{A10})$$

### A.6 Image Scale for Fragmentation Analysis

To calculate image scale, the intersections of all four corner point rays of the image with the 3D model should be determined. For an example image analysis software used to measure fragmentation, Split-Desktop, an image scale is applied at the top and bottom edges of the image. As such, each pair of corner intersection points along each edge are used to compute the image scale for each edge according to Equation A11.

$$\text{image scale} = \frac{\text{image width}}{\sqrt{(\Delta x)^2 + (\Delta y)^2 + (\Delta z)^2}} \quad (\text{A11})$$

Where the image width is the width of the image in pixels, and  $\Delta x, \Delta y$  and  $\Delta z$  are the distances between the corner points along the  $x, y$  and  $z$  world frame axes, respectively. The distance between the corner points is in the unit of distance measurement used in the image analysis software (e.g. meters).